PROCEEDINGS, 51st Workshop on Geothermal Reservoir Engineering
Stanford University, Stanford, California, February 9-11, 2026
SGP-TR-230

Field-Scale Fracture Characterization in Enhanced Geothermal Systems (EGS) Using Streamline-Based Inversion

Takuto Sakai, Akhil Datta-Gupta

Texas A&M University College of Engineering, 3127 TAMU, College Station, TX 77843-3127

takuto.s@tamu.edu

Keywords: enhanced geothermal systems, Utah FORGE, streamline, fracture characterization, inverse modeling

ABSTRACT

Geothermal energy is a readily dispatchable energy source, unlike intermittent renewable energy such as wind and solar, and represents a vital component of a sustainable energy strategy. In Enhanced Geothermal Systems (EGS), hydraulic stimulation creates new fractures and enhances natural ones, enabling heat extraction from formations with limited inherent permeability and working fluids. Because fluid flow in EGS is largely confined to fractures, characterization of fracture properties using dynamic field data is crucial for reliable performance prediction. We propose a novel and rapid streamline-based inversion framework for fracture characterization in EGS.

In this paper, the streamline-based technology, well established in the oil and gas industry, is tailored for EGS applications and introduced for geothermal systems. The proposed framework integrates distributed temperature sensing (DTS) and cluster-level distributed flow rate measurements to calibrate fracture properties. The concept of thermal tracer travel time is utilized to integrate DTS data, while the conventional streamline time of flight is applied to cluster-wise flow rate data. Visualization of thermal tracer travel time provides detailed insight into thermal front propagation behavior and thermal breakthrough time which are key indicators for EGS performance assessment. The streamline-based fracture parameter sensitivities can be computed analytically from a single forward simulation, substantially reducing the computational burden of gradient-based minimization of data misfit during history matching process.

The proposed framework is first validated on a synthetic EGS model with DTS and cluster-level production rate measurements. Subsequently, it is applied to the Utah FORGE site using data from a month-long circulation test conducted in August 2024. In both the synthetic and actual field applications, the proposed approach achieved successful history matching through fracture characterization with high computational efficiency. For the Utah FORGE case, the history matching was carried out in approximately one day with 25 iterations and each iteration requiring a single forward simulation. These results demonstrate that streamline-based technology provides a powerful and efficient tool for fracture characterization and visualization of thermal front propagation in EGS.

1. INTRODUCTION

Geothermal energy has attracted significant attention as a low-carbon and renewable resource that can help meet growing energy demand, support net-zero emissions targets, and enable a sustainable energy strategy. Unlike intermittent renewables such as wind and solar, geothermal energy is largely insensitive to weather variability and is therefore well suited for baseload generation. Enhanced geothermal systems (EGS) (Potter et al. 1974, Smith et al. 1973) expand the potential of geothermal energy by mitigating key limitations of conventional geothermal resources, specifically the availability of in situ working fluid and sufficient permeability (hydraulic conductivity). In EGS, hydraulic stimulation increases permeability, enhancing subsurface fluid circulation between wells and improving heat extraction (Horne et al. 2025). Because fractures govern fluid flow and heat extraction in EGS, understanding fracture characteristics is critical for predicting long-term thermal power output and thermal breakthrough time (Chen and Zhao 2020, Fox et al. 2015, Fu et al. 2016, Guo et al. 2016, Wu et al. 2021). Model calibration using dynamic observations during the fluid circulation period, particularly fracture parameter calibration in this case, provides a robust pathway to infer fracture properties (Chen, Yao, et al. 2020). This study presents a practical approach to fracture characterization in EGS based on observed data that are typically available in field operations.

In EGS projects, the key to success is extracting heat uniformly from the reservoir through stimulated fracture networks for long life periods. Accordingly, three important factors should be evaluated: (1) fracture conductivity, (2) connectivity of the fracture network between wells, and (3) conformance of the injected fluid (Cao and Sharma 2023a, Cao and Sharma 2023c). Fracture propagation simulation is widely used to assess conductivity and connectivity, however, the presence of pre-existing natural fractures introduces significant modeling challenges and remains an active area of research (Srinivasan et al. 2025, McClure 2023, Cao and Sharma 2023b, 2023d, Liu et al. 2024). Cao and Sharma (2022) conducted a detailed investigation of the effects of pressure changes within natural fractures during hydraulic fracturing simulations. In addition, Cao and Sharma (2023a) introduced a computationally efficient model that simulates fracture propagation, fluid flow, and heat transfer in geothermal reservoirs containing natural fractures. In the oil and gas industry, reservoir conformance is defined as “the degree to which the injected fluid uniformly displaces the hydrocarbons across the entire reservoir” (Sagbana and Abushaikha 2021). Although the primary interest in geothermal systems is heat extraction rather than hydrocarbon displacement, conformance remains critical for mitigating early thermal breakthrough and extending reservoir life. In this study, streamlines demonstrate its power for visualizing and evaluating these three key factors (conductivity, connectivity, and conformance) in a real field application.

Monitoring and visualizing subsurface fluid transport are essential for understanding reservoir flow dynamics, optimizing oil and gas field-development plans, and designing CO2 injection schedules for geologic CO2 sequestration (Li et al. 2024). Streamlines are integrated curves that are locally tangential to the direction of instantaneous velocity field, and time of flight (TOF) denotes the travel time of a neutral tracer particle along streamlines. Streamline technique has been used in the oil and gas industry since the 1950s and have played a central role in understanding complex subsurface flow patterns (Datta-Gupta and King 2007). Another notable perspective of streamline technique is the streamline-based history matching, a gradient-based inversion workflow in which efficient sensitivity calculations make the approach robust and scalable for field-scale problems. Streamline-based history matching has been successfully applied across a range of field cases and measurement types, including pressure (Chen et al. 2019, Chen, Yang, et al. 2020, Tanaka et al. 2015), water cut (Alvaro et al. 2011, Cheng et al. 2005, He et al. 2002, Yin et al. 2011), gas oil ratio (GOR) (Cheng et al. 2007, Zhang et al. 2025), time lapse seismic (Hetz et al. 2017, Liu et al. 2020, Watanabe et al. 2017), and distributed temperature sensing (DTS) (Yao et al. 2024). In this study, we tailor the streamline-based history matching workflow for geothermal applications by incorporating DTS and distributed flow rate measurements, which are commonly available in EGS operations (Dadi et al. 2024, Holt 2025, Schölderle et al. 2021, Titov et al. 2025, Xing et al. 2025). Using these observed data, we calibrate hydraulic fracture properties. In addition, streamline and the thermal tracer TOF concept proposed by Somogyvári et al. (2016) are suitable tools to visualize injector-producer connectivity and thermal front propagation, including thermal breakthrough time, which is a key metric in geothermal reservoir management (Bjarkason 2023, Ji et al. 2025, Podgorney et al. 2025, Wu et al. 2021, Aladwani et al. 2025). Following model calibration, we demonstrate the potential of these visualization techniques in a real EGS case.

This paper is structured as follows. The methodology section presents the mathematical formulation of streamline, thermal tracer travel time, and streamline-based inversion workflow. We then validate the proposed workflow using a synthetic model. Next, we apply the workflow to a field case from the Utah FORGE project to highlight its robustness and computational efficiency and to illustrate the visualization capability of streamline and thermal tracer TOF. Finally, the paper concludes with a summary of key findings.

2. METHODOLOGY

This section presents the mathematical formulation of thermal tracer travel time, an overview of the streamline-based inversion workflow, the data misfit calculations, and streamline-based efficient sensitivity calculations. The latter two components are essential to the streamline-based inversion procedure.

2.1 Thermal tracer travel time

Based on the concepts of streamline and time of flight (TOF), we introduce thermal tracer travel time (i.e., thermal tracer TOF) by incorporating a thermal retardation factor. This section presents the mathematical formulation of these concepts.

A streamline is an instantaneous lines that are everywhere tangential to a velocity field, and TOF represents the travel time of a neutral tracer particle along a streamline (Datta-Gupta and King 2007). Following the streamline tracing algorithm proposed by Pollock (1988), and assuming that each velocity component varies linearly within a grid cell along its corresponding coordinate direction and is independent of the other components, streamlines can be traced from a specified starting point (e.g., an injector). Once the streamlines are traced, TOF is computed by integration along the streamline. Specifically, the TOF, τ, along a streamline ψ is expressed as

$$\tau = \int_{\psi} \frac{\phi(r)}{u(r)} dr \tag{1}$$

where $\phi(r)$ is the porosity, $u(r)$ is the Darcy velocity, and dr is the distance element along the streamline. In this work, a commercial reservoir simulator is used to compute the velocity field, from which streamlines are traced and TOF is calculated along each streamline.

Temperature propagation is governed by the energy conservation equation. Under the assumption of negligible heat conduction (advection-dominated heat transport), the energy conservation equation admits an analytical solution, yielding the relationship between the thermal front velocity, u_{th}, and the Darcy velocity, u (Grant and Bixley 2011), as

$$u_{th} = \frac{\rho_w C_w}{\rho_t C_t} u = \frac{\rho_w C_w \phi}{\rho_t C_t} u_{pore} \tag{2}$$

$$\rho_t C_t = \phi \rho_w C_w + (1-\phi)\rho_r C_r \tag{3}$$

where u_{pore} is the pore velocity, ρ_w is the water density, ρ_t is the total density, ρ_r is the rock density, C_w is the water specific heat, C_t is the total specific heat, and C_r is the rock specific heat. Based on Equation-(2), the thermal retardation factor, R, is defined as

$$R = \frac{u_{pore}}{u_{th}} = \frac{\rho_t C_t}{\phi \rho_w C_w} \tag{4}$$

By incorporating the thermal retardation factor into Equation-(1), the thermal tracer travel time is expressed as follows (Somogyvári et al. 2016). This factor accounts for the slower propagation of the thermal front relative to a neutral tracer particle.

$$\tau_{tt} = \int_{\psi} \frac{R(r)\phi(r)}{u(r)} dr \tag{5}$$

In this work, thermal tracer travel time is used for sensitivity calculations to integrate DTS data, whereas conventional TOF is used for distributed flow rate data. Thermal tracer travel time also plays a key role in visualizing thermal front propagation and predicting thermal breakthrough time.

2.2 Overview of streamline-based inversion workflow

An overview of the streamline-based inversion workflow is shown in Figure 1, and further details are provided by Datta-Gupta and King (2007) and He et al. (2002). As illustrated in Figure 1, the workflow starts from a prior model and calibrates model parameters through an iterative process. At each iteration, streamline-based sensitivities of reservoir properties to the target monitoring data are computed and used to update the model parameters until the misfit between observed data and simulated well responses falls within an acceptable range. In this study, the workflow is tailored to EGS applications by integrating DTS data and distributed flow rate measurements as dynamic observations. A notable advantage of the streamline-based approach is that sensitivities can be computed analytically from a single forward simulation, whereas alternative inversion methods, such as evolutionary algorithms or ensemble-based data assimilation, typically require a large number of forward simulations. The objective function for the inverse problem is defined as follows.

$$J(\delta \boldsymbol{R}) = \|\delta \boldsymbol{d} - \boldsymbol{G}\delta \boldsymbol{R}\| + \beta_1 \|\delta \boldsymbol{R}\| + \beta_2 \|\boldsymbol{L}\delta \boldsymbol{R}\| \tag{6}$$

where $J(\delta \boldsymbol{R})$ is the objective function, $\delta \boldsymbol{d}$ is the data misfit vector, $\boldsymbol{G}$ is the sensitivity matrix with respect to the reservoir cell properties, and $\delta \boldsymbol{R}$ denotes the parameter update. In this study, $\delta \boldsymbol{R}$ corresponds to updates in cell permeability. The second term, the norm constraint, penalizes deviations from the prior model to preserve the prior geologic information, with β_1 controlling the strength of this regularization. The third term, the smoothness constraint, penalizes unphysically sharp spatial variations in the parameters, $\boldsymbol{L}$ is the second-order spatial difference operator (Laplacian matrix), and β_2 is the corresponding regularization weight. Although selection of the tuning parameters can be subjective, guidelines for choosing β_1 and β_2 are discussed by Parker (1994). Equation-(6) can be reformulated as an augmented linear system as follows.

$$\begin{pmatrix} \boldsymbol{G} \\ \beta_1 \boldsymbol{I} \\ \beta_2 \boldsymbol{L} \end{pmatrix} \delta \boldsymbol{R} = \begin{pmatrix} \delta \boldsymbol{d} \\ 0 \\ 0 \end{pmatrix} \tag{7}$$

The augmented linear system in Equation-(7) is solved using the iterative Least Squares solver LSQR (Paige and Saunders 1982), yielding $\delta \boldsymbol{R}$, the update to the reservoir property field. The overall workflow is iterative process, at each iteration, Equation-(7) is solved to update the model parameters, after which a forward simulation is performed using the updated properties. Streamlines are then traced and streamline-based sensitivities are computed from this single forward simulation. The updated misfit and sensitivity matrix are used to reassemble Equation-(7), which is subsequently solved again with LSQR. This cycle is repeated until the data misfit decreases below a prespecified tolerance (Figure 1). The key components of the workflow are the definitions of the data misfit vector, $\delta \boldsymbol{d}$, and the sensitivity matrix, $\boldsymbol{G}$, in Equation-(7). Their formulations are presented in the following sections.

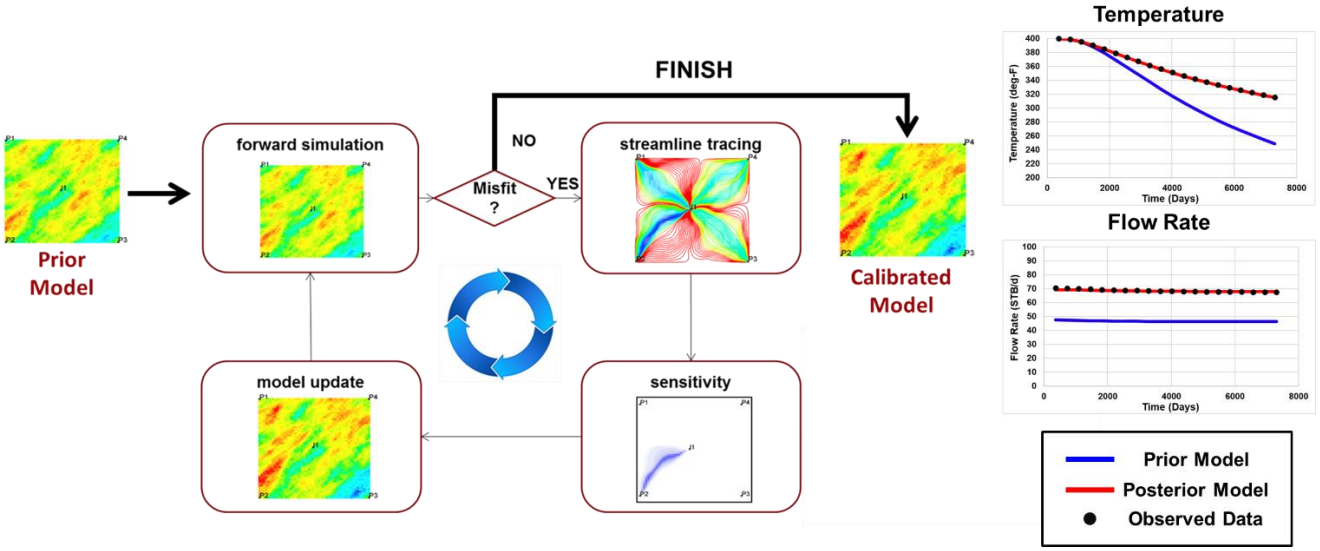

Figure 1. Diagram of streamline-based inversion workflow

2.3 Data misfit calculations

This section describes the data misfit formulation between observed and simulated responses, which constitutes the $\delta \boldsymbol{d}$ term in Equation-(7) used to compute reservoir property updates. Section 2.3.1 presents the misfit definition for DTS data, and section 2.3.2 presents the misfit definition for distributed flow rate measurements.

2.3.1 Data misfit calculation for DTS data

The misfit for DTS data is evaluated using the generalized travel time (GTT) concept. GTT-based misfit formulations have been applied in a range of field applications, including water-cut data (Alvaro et al. 2011, Cheng et al. 2005, He et al. 2002, Yin et al. 2011), gas–oil ratio (GOR) data (Cheng et al. 2007, Zhang et al. 2025), and time-lapse seismic data (Hetz et al. 2017, Liu et al. 2020, Watanabe et al. 2017), demonstrating robustness and computational efficiency. Yao et al. (2024) further extended the approach to DTS data in geologic CO2 sequestration applications. The GTT misfit is defined as the time shift that minimizes the difference between simulated and observed responses. Operationally, the simulated response is shifted over a set of candidate time shifts, and the misfit is evaluated for each shift, then the shift that yields the minimum misfit is taken as the GTT misfit (Figure 2). For a given time shift, the misfit is computed by aggregating pointwise differences over all time samples, as follows.

$$GTT\ misfit(\Delta t) = \sum [y^{cal}(t_i + \Delta t) - y^{obs}(t_i)]^2 \tag{8}$$

where, $y^{cal}(t_i + \Delta t)$ is simulated responses shifted by Δt from t_i, and $y^{obs}(t_i)$ is observed data at t_i. The advantage of using GTT-based misfit rather than amplitude matching is that GTT formulation reduces nonlinearity and can improve convergence of the inverse problem (Cheng et al. 2005). For the DTS application, a single GTT-based misfit is computed independently at each sensor location, yielding a set of pointwise misfits (misfit vector) across the distributed measurement points.

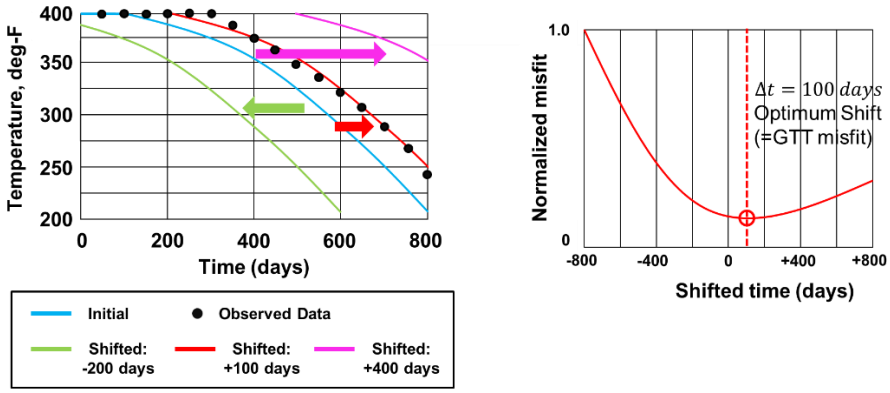

Figure 2. Calculation of GTT misfit for DTS data

2.3.2 Data misfit calculation for distributed flow rate data

Consistent with the data misfit formulation used for bottomhole pressure in streamline-based inversion workflow (Chen et al. 2019, Chen, Yang, et al. 2020, Tanaka et al. 2015), the flow rate misfit is defined as the difference between simulated and observed flow rates, averaged over the number of time samples (Figure 3). Similar to the GTT-based DTS misfit, this time-averaging yields a single misfit value for each distributed measurement point (e.g., each cluster).

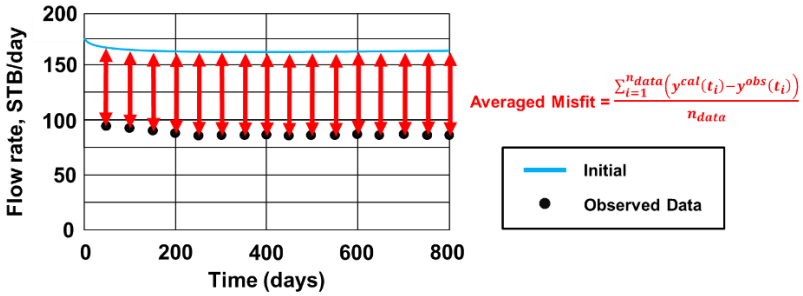

Figure 3. Calculation of misfit for flow rate data

2.4 Streamline-based sensitivity calculations

As mentioned earlier, the streamline-based inversion workflow efficiently computes sensitivities of reservoir properties to the observed data, here DTS data and distributed flow rate measurements, from a single forward simulation. Section 2.4.1 presents the mathematical formulation for sensitivities associated with DTS data using the thermal tracer travel time concept, whereas section 2.4.2 describes the sensitivity calculation for distributed flow rate data.

2.4.1 Sensitivity calculation for DTS data

The formulation to calculate sensitivity for DTS data follows the one introduced by Yao et al. (2024) for geologic CO2 sequestration. The streamline-based sensitivity expressions are derived by introducing the concept of slowness, defined as the reciprocal of the thermal tracer velocity. The thermal tracer velocity is obtained by applying the thermal retardation factor discussed in section 2.1. Using Darcy's law, the slowness can be expressed as follows.

$$s_{tt}(x) = \frac{\phi(x)}{R(x)\lambda_{rt}k(x)|\nabla P|} \tag{9}$$

where λ_{rt} is total relative mobility and $|\nabla P|$ is pressure gradient. The partial derivative of slowness with respect to permeability is given in Equation-(10). This derivation assumes that streamlines are not significantly changed by a local perturbation in permeability.

$$\frac{\partial s_{tt}(x)}{\partial k(x)} \approx \frac{-\phi(x)}{R(x)\lambda_{rt}\big(k(x)\big)^2|\nabla P|} = -\frac{s_{tt}(x)}{k(x)} \tag{10}$$

Since the thermal tracer travel time, $\delta\tau_{tt}$, is obtained by integrating slowness along a streamline ψ, it can be written as

$$\delta\tau_{tt}(\psi) = \int_{\psi} \delta s_{tt}(r)dr = \delta s_{tt}(x)\Delta r(x) \tag{11}$$

From Equation-(10) and (11), the streamline-based sensitivity (i.e., thermal tracer travel time sensitivity along a streamline ψ) with respect to the permeability of grid cell x is given by

$$\frac{\delta\tau_{tt}(\psi)}{\delta k(x)} = \frac{\delta s_{tt}(x)\Delta r(x)}{\delta k(x)} = -\frac{s_{tt}(x)\Delta r(x)}{k(x)} = -\frac{\Delta\tau_{tt}(x)}{k(x)} \tag{12}$$

where $\Delta r(x)$ is the arc length of the streamline segment within the grid cell at x and $\Delta\tau_{tt}(x)$ is the travel time which thermal tracer requires to travel along this streamline segment. As shown in Equation-(12), tracing streamlines and computing thermal tracer TOF for each streamline segment enables efficient evaluation of sensitivities of reservoir cell properties to thermal tracer travel time from a single forward simulation.

2.4.2 Sensitivity calculation for distributed flow rate data

Horizontal wells are commonly used in EGS designs, and reservoir properties along a streamline influence flow allocation among production locations along the horizontal well. This section introduces a novel formulation for sensitivities associated with distributed flow rate measurements.

Figure 4 shows a schematic of streamlines for horizontal well configuration. Each streamline is divided into segments according to the underlying grid. Darcy's law is assumed to hold for each streamline segment, and Equation-(13) expresses Darcy's law for segment-i.

$$q_i^{sln} = -\frac{A_i\lambda_{t,i}k_i}{L_i}\left(\Delta P_i^{sln} - \overline{\rho_i}gD_i\right) \tag{13}$$

where, q_i^{sln} is flow rate of streamline segment-*i*, A_i is area of streamline segment-*i*, k_i is permeability of streamline segment-*i*, L_i is length of streamline segment-*i*, $\lambda_{t,i}$ is total relative mobility of streamline segment-*i*, $\overline{\rho_i}$ is average density of flowing fluid of streamline segment-*i*, D_i is depth difference of streamline segment-*i*, g is gravitational constant, and ΔP_i^{sln} is pressure drop of streamline segment-*i*. Differentiating q_i^{sln} in Equation-(13) with respect to the permeability of the underlying cell, k_i, yields the flow rate sensitivity with respect to permeability, $sens_i^q$, as follows.

$$sens_i^q = \frac{\partial q_i^{sln}}{\partial k_i} = -\frac{A_i\lambda_{t,i}}{L_i}\left(\Delta P_i^{sln} - \overline{\rho_i}gD_i\right) \tag{14}$$

In Equation-(14), calculation of the sensitivity requires the pressure drop across each streamline segment. This pressure drop is obtained by interpolating pressures from the surrounding grid blocks using the procedure described by Chen et al. (2019).

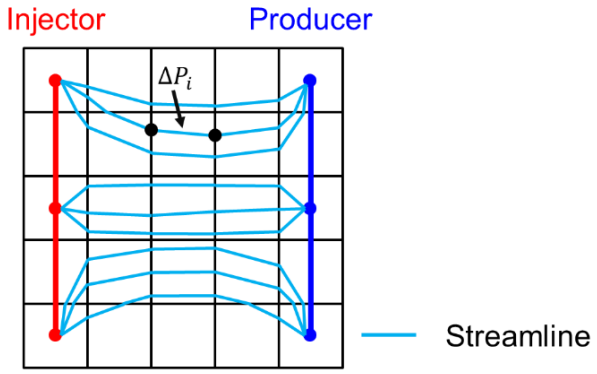

Figure 4. Schematic of streamlines in horizontal well design

3. VALIDATION USING SYNTHETIC CASE APPLICATION

The proposed workflow is applied to a synthetic case to validate its performance. This section describes the synthetic model setup and the results.

3.1 Model description

Figure 5 shows a two-dimensional synthetic reservoir model designed to mimic key EGS reservoir characteristics. A single layer is extracted from a three-dimensional field-scale model presented by Chan, Datta-Gupta, et al. (2025), details of the original model are provided therein. The dimension of the synthetic model is $400 \times 560 \times 1$ and the reservoir size is 2,000 ft × 2,800 ft with a thickness of 30 ft. The top of the model is at a depth of 8,485 ft. Rock properties are based on an Eagle Ford shale reservoir (Yang et al. 2017). The background permeability is very low, and nonuniform with 20 hydraulic fractures included. A nonplanar, complex hydraulic fracture network is generated using a commercial fracture propagation simulator and represented on a high-resolution structured grid. Fracture permeability is heterogeneous and ranges from 0.008 to 250 mD. The model has a triplet horizontal well system, consisting of one horizontal injector located between two horizontal producers. These wells are hydraulically connected through the fracture network, as shown in Figure 5. Thermal properties are summarized in Table 1. Thermodynamic properties of water and steam are computed using the IAPWS-IF97 (Wagner et al. 2000) which is industrial analytical formulation. The initial reservoir pressure and temperature are 2,900 psi and 400 °F, respectively, throughout the model. Cold water at 50 °F is injected at a constant rate of 400 STB/day, while both producers operate under a constant bottomhole pressure of 2,175 psi. The simulation period is 20 years.

Each producer contains 20 perforated grid cells connected to the fracture network. For these perforated cells, we assume distributed temperature and flow rate measurements as synthetic observation dataset. The synthetic dataset is generated by running the commercial compositional reservoir simulator Eclipse™ (E300) (SLB 2023) for 20 years. Time-series temperature and flow rate responses are then extracted for the 40 perforated cells (20 per producer) and used as the synthetic observed data.

Table 1: Thermal properties of a synthetic model

Thermal properties	Unit	Values
Rock heat capacity	$\mathrm{Btu/ft^3/°R}$	32.393
Rock thermal conductivity	Btu/ft/°R	42.32
Water thermal conductivity	Btu/ft/°R	9.7132

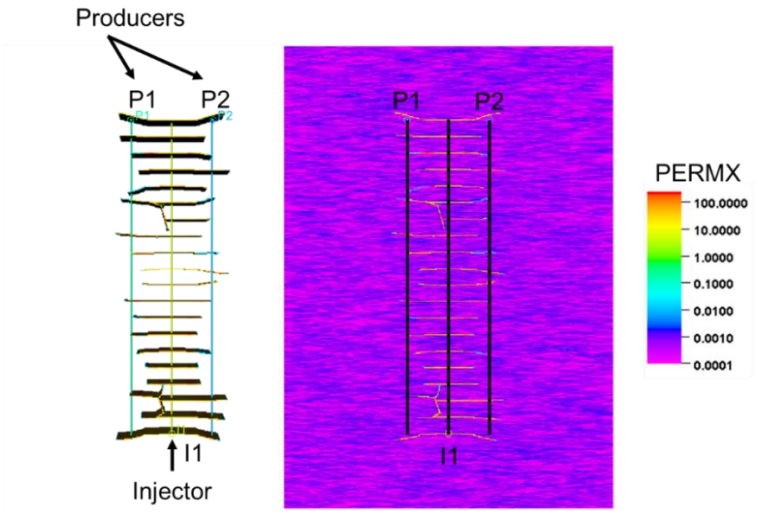

Figure 5. A 2D synthetic model permeability distribution and well designs

3.2 Application results

As prior model for the inversion, a homogeneous fracture permeability is assumed, with a value of 50 mD assigned to all fracture cells. Starting from this prior model, the proposed streamline-based inversion workflow is applied to the synthetic case. The inversion is performed for nine iterations, calibrating fracture permeability based on the synthetic distributed temperature and flow rate data at the target cells along the two producers discussed in section 3.1. Detailed results are presented in the following sections.

3.2.1 Inversion results: distributed temperature responses

Figure 6 summarizes the inversion results for the distributed temperature data. Figure 6-(a) and (b) compare the temperature onset time along producers P1 and P2, respectively. Here, temperature onset time is defined as the time at which the temperature drop exceeds a prespecified threshold (10 °F in this study). This concept is used to visualize the agreement among the prior model (blue), posterior model (red), and synthetic observed data (black markers) at multiple target cells along the producers in a single figure. The results indicate great matching performance for both P1 and P2 after inversion. Figure 6-(c) shows the normalized misfit over iterations, indicating a monotonic decrease and a reduction to approximately 10% of the initial misfit after nine iterations. For additional detail, Figure 6-(d) compares the time-series temperature responses at cell-6 of P2 for the prior model (blue), posterior model (red), and observed data (black dashed line). At this location, the prior model predicts an early temperature decline exceeding 10 °F, whereas the posterior model shows almost no decline over the simulation period, consistent with the observations. Accordingly, the onset time at cell-6 is early for the prior model but equals the simulation end time for the posterior model in Figure 6-(b).

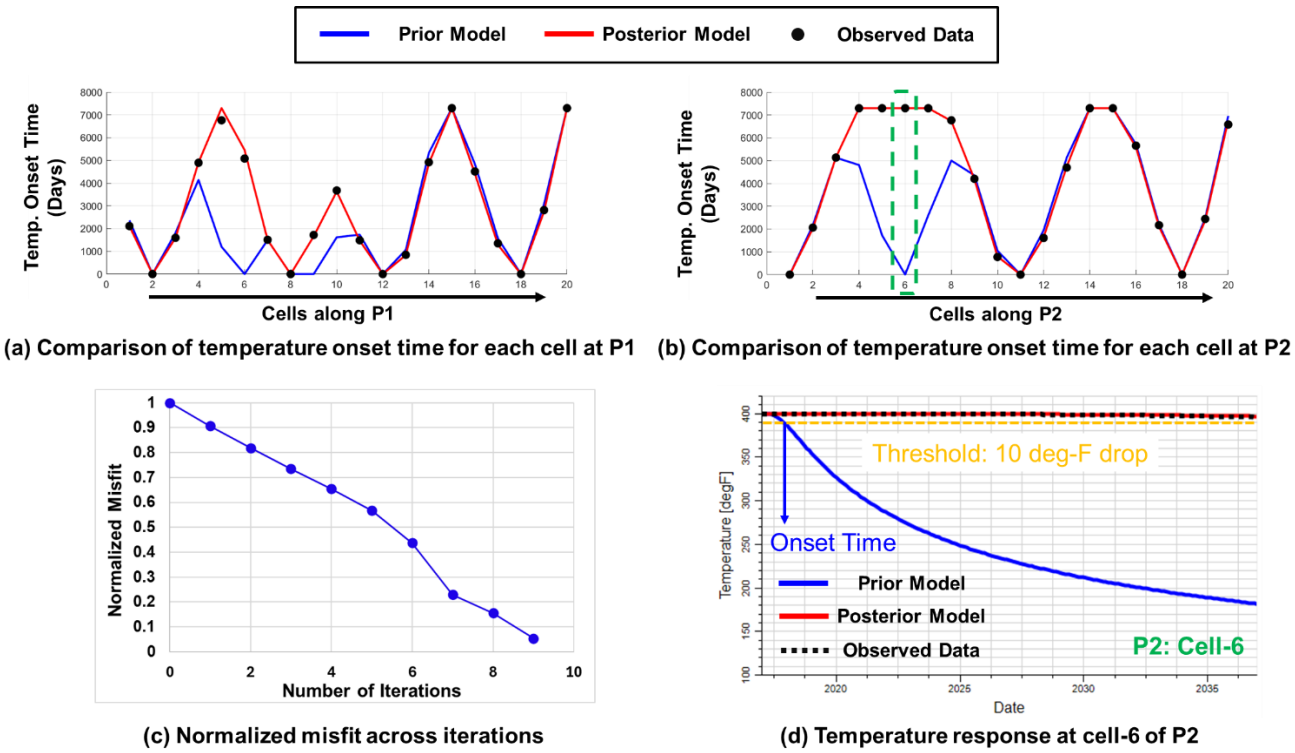

(a) Comparison of temperature onset time for each cell at P1

(b) Comparison of temperature onset time for each cell at P2

(c) Normalized misfit across iterations

(d) Temperature response at cell-6 of P2

Figure 6. Summary of inversion results for distributed temperature responses in the synthetic case

3.2.2 Inversion results: distributed flow rate responses

Next, we present the inversion results for the distributed flow rate responses. Figure 7 summarizes the results, and Figure 7-(a) and (b) compare the time-averaged flow rate at each target cell along P1 and P2, respectively. Time-averaged flow rate is used to visualize the agreement of distributed flow rate responses among the prior model (blue), posterior model (red), and observed data (black markers) at multiple locations along the producers, in a single figure. The posterior model shows great agreement with the observed data, indicating that the inferred flow allocation among cells is consistent with the synthetic observed data. Figure 7-(c) shows the normalized misfit over iterations, exhibiting a monotonic decrease to approximately 10% of the initial misfit after nine iterations, consistent with the temperature data results (section 3.2.1). Figure 7-(d) provides a representative example by comparing the time-series flow rate at cell-2 of P1 for the prior model (blue), posterior model (red), and observed data (black dashed line), further confirming the improved match after inversion.

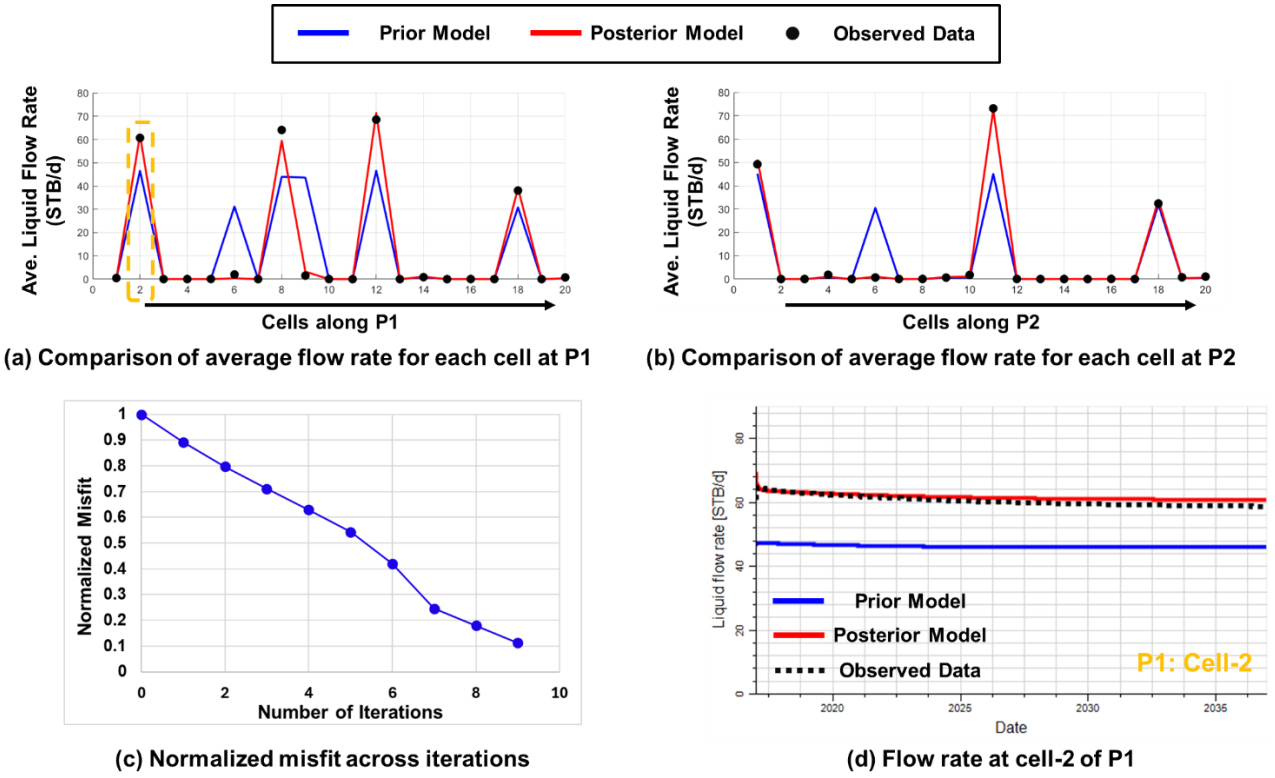

Figure 7. Summary of inversion results for distributed flow rate responses in the synthetic case

3.2.3 Inversion results: permeability changes

The left-hand side of Figure 8 shows permeability updates obtained from the inversion process, where positive changes are shown in red and negative changes in blue. The right-hand side of Figure 8 presents times-series temperature responses at cell-9 of P1 and cell-11 of P2. As indicated on the left-hand side, the permeability of the fracture connecting to cell-9 of P1 decreases during inversion, which delays the simulated temperature decline and improves agreement with the observed data (top-right). In contrast, the permeability of the fracture connecting to cell-11 of P2 increases, facilitating the simulated temperature decline and improving agreement with the observed data (bottom-right). These results indicate that the streamline-based inversion calibrates fracture permeability in a physically reasonable manner guided by the efficiently computed sensitivities. Overall, the synthetic 2D model validates the proposed inversion workflow for both distributed temperature and distributed flow rate data.

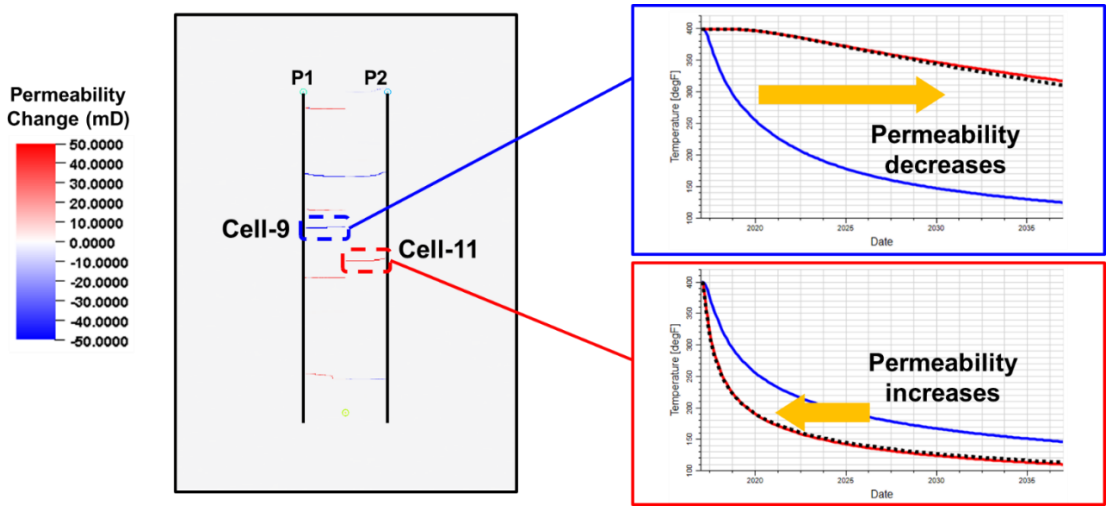

Figure 8. Permeability changes after model calibration for the synthetic case

4. FIELD APPLICATION: UTAH FRONTIER OBSERVATORY FOR RESEARCH IN GEOTHERMAL ENERGY (FORGE) PROJECT

After validating the proposed workflow on the synthetic case, we apply it to the Utah FORGE (Frontier Observatory for Research in Geothermal Energy) field case to demonstrate robustness and computational efficiency of the streamline-based inversion workflow. This section presents and discusses the inversion results along with streamline-based visualization for the Utah FORGE case.

4.1 Overview of Utah FORGE project

The Utah FORGE project is the largest EGS demonstration site and is funded by the U.S. Department of Energy. The site, located approximately 16 km northeast of Milford, Utah, is well suited for EGS development and consists of granite and gneiss with temperatures of approximately 175 to 225 °C at depths of 2 to 4 km (Allis et al. 2016). The project includes two deviated wells, 16A(78)-32 (injector) and 16B(78)-32 (producer), with the producer located approximately 300 ft above the injector. Multistage hydraulic stimulation was conducted in 16A(78)-32 to create a stimulated fracture network comprising 10 stages with cluster spacing of 45 to 75 ft (Kumawat et al. 2025, Liu et al. 2025), while 16B(78)-32 includes five stages to produce the injected fluid (England et al. 2024).

At the Utah FORGE site, a series of hydraulic stimulation and fluid circulation tests have been conducted. In August 2024, a month-long circulation test was performed in which water was injected into well 16A(78)-32 and produced from well 16B(78)-32. The test reported a high mass recovery (approximately 90%) and high produced fluid temperatures (England et al. 2024). During the circulation test, water was circulated between the wells at approximately 10 bpm. A production logging tool (PLT) survey in 16B(78)-32 provided cluster-wise inflow distribution. In addition, fiber-optic cables installed in the annulus of well 16B(78)-32 (Liu et al. 2025) enabled DTS measurements during the test (Jurick and Guzik 2024). A more detailed description of the available monitoring data is provided in the following sections. This study focuses on the August 2024 circulation test and applies the proposed inversion workflow to assimilate the observed flow rate data to calibrate hydraulic fracture permeabilities.

4.2 Available monitoring data from circulation test

4.2.1 Distributed temperature sensor (DTS) data

As mentioned above, DTS data were acquired during the circulation test and are available from the Geothermal Data Repository (https://gdr.openei.org/submissions/1721). Figure 9 displays the DTS measurements. The dataset covers only a limited time interval (August 12, 2024, 7:00 pm to August 16, 2024, 2:00 pm), whereas the circulation test lasted approximately one month. In addition, because the available DTS window begins several days after the start of circulation (August 8, 2024) and spans only four days, the thermal signal associated with the cold-water injection is not yet clearly observed in the DTS record. Given the limited temporal coverage and weak temperature response, the DTS data provides insufficient dynamic information to constrain fracture properties for this study. Therefore, DTS data is not included as an observed data in this application.

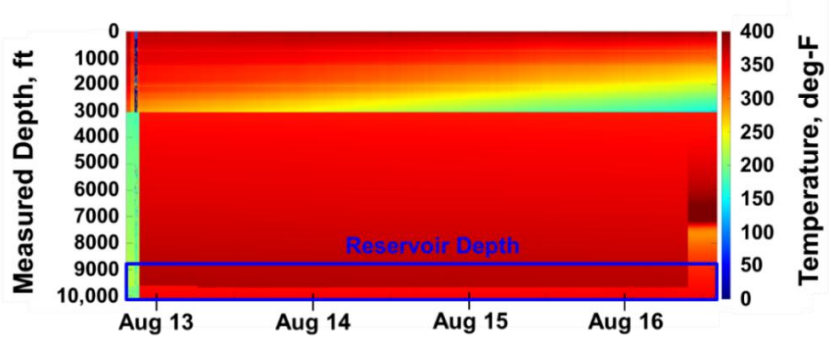

Figure 9. DTS data from one-month circulation test based on data from Jurick and Guzik (2024)

4.2.2 Distributed flow rate data

Based on the interpretation of the PLT survey reported by England et al. (2024), cluster-wise inflow distributions for well 16B(78)-32 are provided in their report. Table 2 and Figure 10 summarizes this information. Perforation clusters in Stages 5 and 4 are labeled as 5.1, 5.2, 5.3, 5.4 and 4.1, 4.2, 4.3, 4.4, respectively, and the inflow contributions from Stages 1 through 3 are aggregated into a single cluster. Thus, inflow fractions are available for nine clusters in total (Figure 10). These inflow fractions were measured during the PLT survey conducted on August 26, 2024. In this study, we assume that the inflow fractions remain constant over the entire circulation test. Time-series target flow rates for each cluster are then computed by multiplying the total production rate by the corresponding cluster inflow fraction. These cluster-level time-series flow rate are used as observed data in the inversion to calibrate fracture properties for the field application.

Table 2: Cluster-wise inflow distribution for well 16B(78)-32 based on the PLT survey from England et al. (2024)

Stage	Perforations		Water (%)
5.1 (Cluster-1)	8774	8778	0.2
5.2 (Cluster-2)	8834	8838	10.8
5.3 (Cluster-3)	8870	8874	2.6
5.4 (Cluster-4)	8879	8883	12.3
4.1 (Cluster-5)	8958	8962	11.4
4.2 (Cluster-6)	8995	8999	6.3
4.3 (Cluster-7)	9026	9030	11.9
4.3 (Cluster-8)	9054	9058	8.2
3 (Cluster-9)	Below 9240		36.3
2 (Cluster-9)			
1 (Cluster-9)			

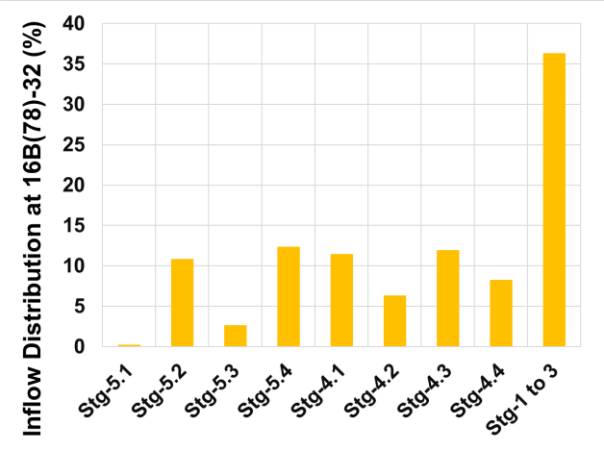

Figure 10. Inflow distribution summary for 16B(78)-32 based on data from England et al. (2024)

4.3 Prior dynamic model

Chan, Kumawat, et al. (2025) developed a dynamic reservoir simulation model for Utah FORGE based on a discrete fracture network (DFN) constructed from well-log interpretations and micro-seismic monitoring data (Finnila and Jones 2024), together with an initial state model (Podgorney 2020). They further performed history matching using injector and producer bottomhole pressure data from the month-long circulation test. Based on Distributed Strain Sensor (DSS) measurements acquired in well 16B(78)-32 (Jurick 2024), Kumawat et al. (2025) identified fracture corridor region with a high likelihood of containing hydraulic fractures. Chan, Kumawat, et al. (2025) then calibrated permeability and porosity multipliers for this fracture corridor region, as well as well index multipliers for the injector and producer, during the history matching process. In this study, the resulting model is used as the prior model. We further calibrate cell-based permeability within the fracture corridor region by assimilating cluster-level distributed flow rate data along well 16B(78)-32. Additional details of the prior model are provided by Chan, Kumawat, et al. (2025).

4.4 Inversion results

Using the pre-history-matched model based on injector/producer bottomhole pressure data as discussed in section 4.3 as the prior model, we apply the streamline-based inversion workflow to calibrate cell-based permeabilities within the fracture corridor region identified from the DSS analysis. The calibration uses the observed cluster-wise inflow distribution for well 16B(78)-32. As described in section 4.2.2, well 16B(78)-32 contains nine clusters with available inflow fraction measurements. For the field application, the inversion is run for 25 iterations. Each iteration requires only a single forward reservoir simulation. In this case, a forward run takes approximately 1 hour using the commercial compositional simulator Eclipse™ (E300) (SLB 2023), and the entire process completes in approximately one day. Figure 11 summarizes the inversion results. Figure 11-(a) compares the cluster-wise inflow distribution for well 16B(78)-32 among the prior model (blue), posterior model (red), and observed data (black markers), showing improved agreement across all clusters after inversion. Figure 11-(b) shows the normalized misfit over iterations, indicating a monotonically decreasing trend. The misfit reaches approximately 10% of its initial value within the first 10 iterations, corresponding to roughly 10 hours of computation. Figure 11-(c), (d), and (e) provide representative time-series comparisons for cluster-2, 4, and 9, further illustrating the improved match obtained by the inversion. Overall, these results demonstrate that the proposed workflow achieves efficient and robust calibration of fracture permeability using cluster-level inflow distribution data.

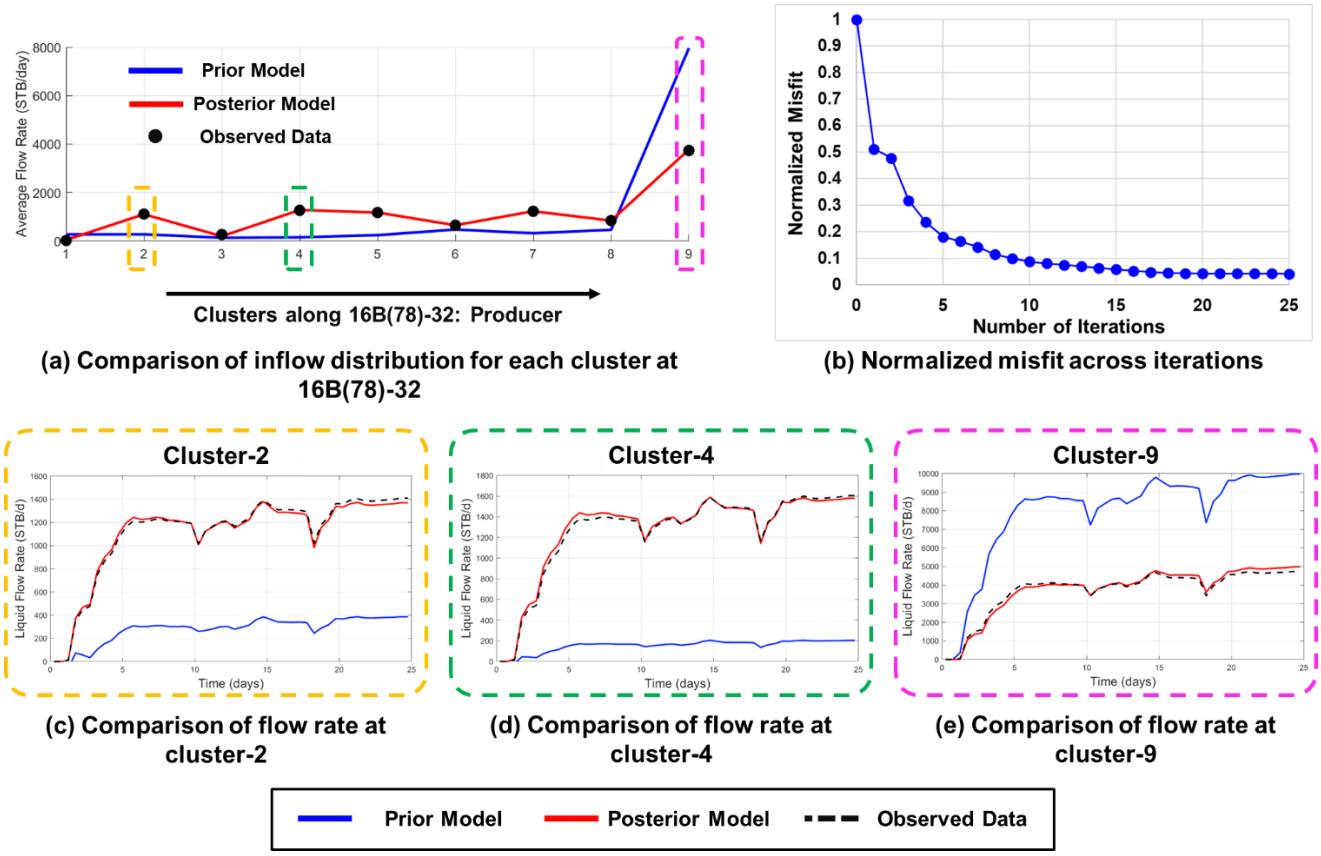

Figure 11. Summary of inversion results for the Utah FORGE case

4.5 Visualization and analysis of inversion results using streamlines

In this section, we use the streamline and the thermal tracer TOF concept to visualize the inversion results. The streamline visualizations demonstrate their utility for evaluating three key EGS factors introduced earlier: fracture conductivity, connectivity, and flow conformance.

To illustrate how fracture conductivity is calibrated, Figure 12 shows cell-based permeability updates obtained during the inversion for the Utah FORGE case. The left-hand plot highlights positive permeability changes, whereas the right-hand plot highlights negative changes. Together, these permeability updates delineate preferential flow paths inferred by the inversion workflow.

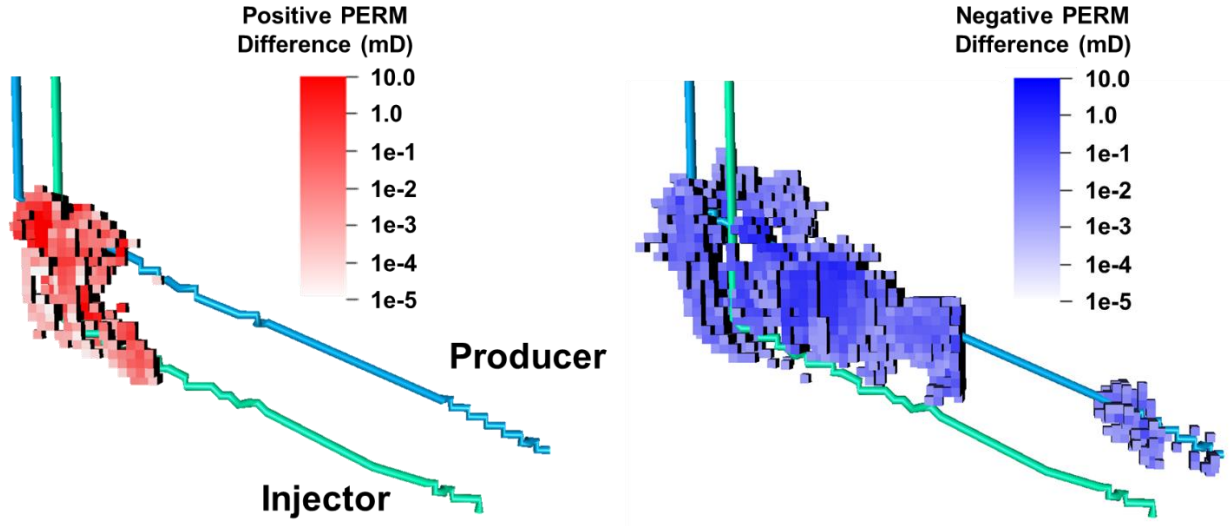

Figure 12. Permeability updates after model calibration for the Utah FORGE case

Next, to illustrate how connectivity changes during model calibration, Figure 13 compares streamlines in the prior and posterior models. Streamlines are colored by their destination cluster, enabling visualization of changes in injector-producer flow connectivity and cluster-level flow allocation. The posterior model streamlines are redirected along the preferential flow paths identified from the permeability updates (Figure 12), indicating connectivity changes induced by calibration. Because streamline color denotes the destination cluster, Figure 13 also shows how flow partitioning among clusters changes after calibration. Specifically, the right-hand figure (posterior model) shows a larger fraction of streamlines terminating at clusters 4, 5, and 7 (green, light blue, and pink) and fewer streamlines terminating at cluster-9 (gray), consistent with the corresponding changes in inflow fractions in the posterior model as shown in Figure 11.

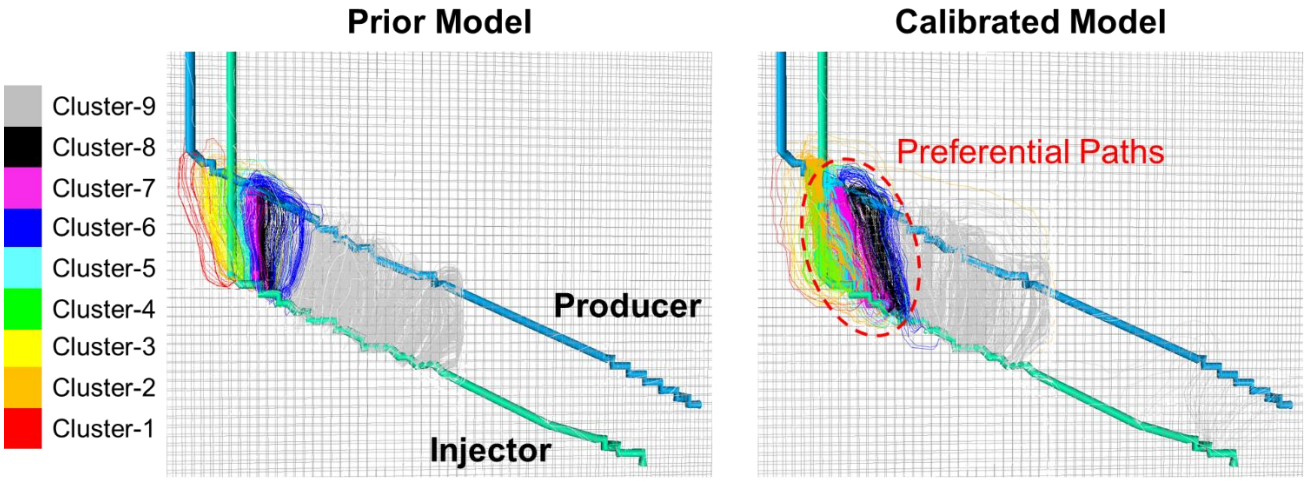

Figure 13. Visualization of connectivity changes using streamlines

Figure 14 visualizes thermal tracer travel time along streamlines for the prior and posterior models, representing the propagation time of the thermal front from the injector. This visualization enables assessment of the spatial uniformity of thermal front propagation and how it changes with model calibration, which directly relates to the uniformity of heat extraction from the reservoir. Thermal tracer travel time can be interpreted as an estimate of thermal breakthrough time, a key performance metric in EGS operations. Because travel time of thermal tracer can be predicted beyond the simulated time window, thermal breakthrough timing can be assessed from shorter-duration numerical simulations without extending simulation period, improving computational efficiency. Overall, the thermal tracer travel time visualization demonstrates its utility for evaluating flow conformance in EGS.

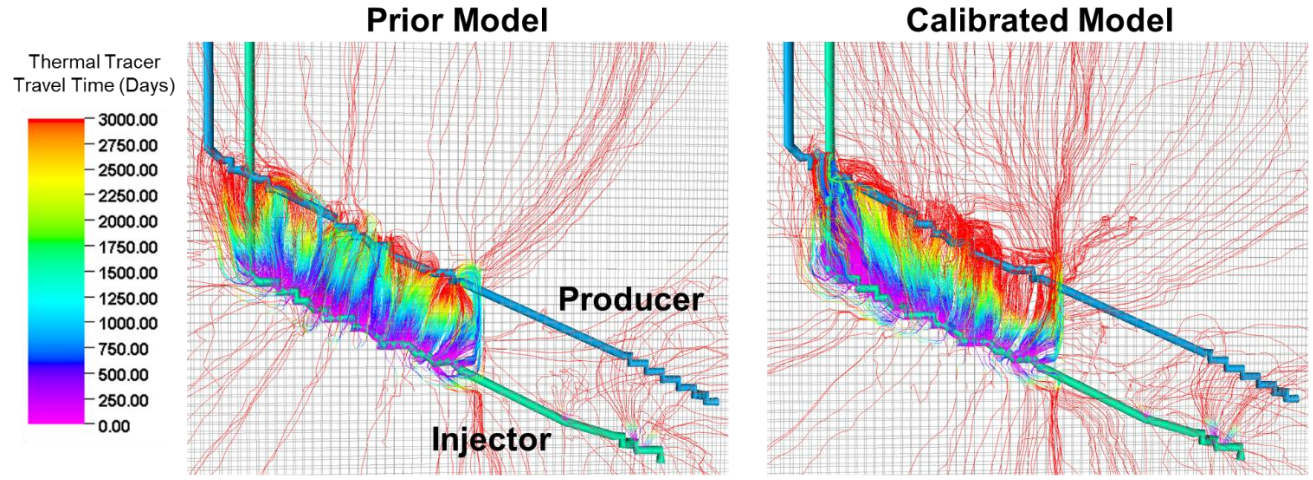

Figure 14. Visualization of thermal tracer travel time along streamlines

Figure 15 visualizes thermal front propagation on the grid system. For each grid cell, the travel time is defined as the minimum thermal tracer travel time among all streamlines that pass through the cell of interest. By filtering cells using selected travel time thresholds (100, 1000, 1500, 2500, 4000, and 5000 days in Figure 15), thermal front propagation can be visualized, providing insight into the evolution of the thermal front.

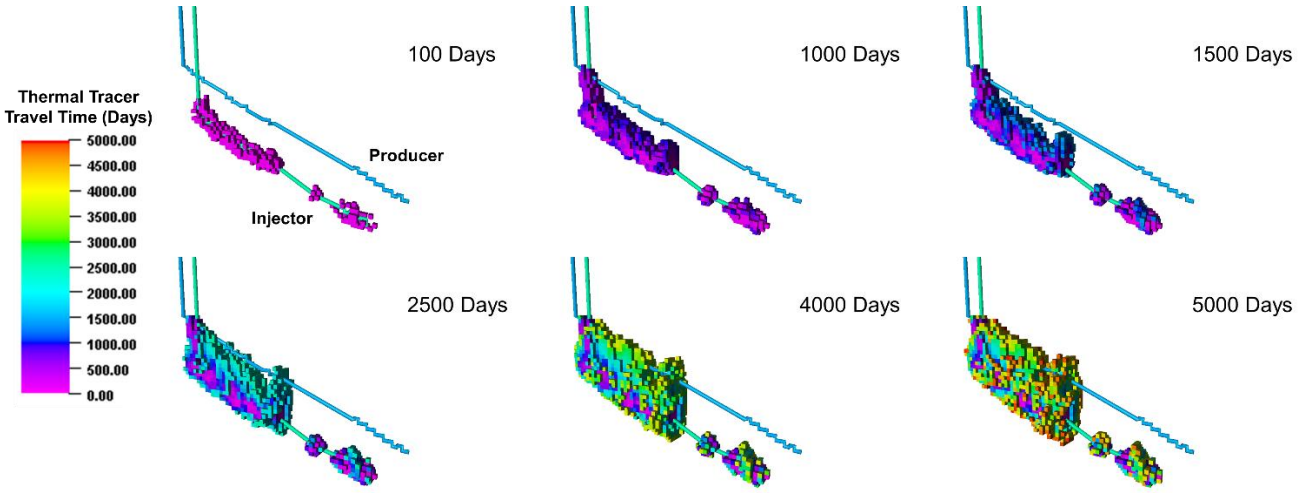

Figure 15. Visualization of thermal propagation front

This visualization capability demonstrates that streamlines and travel time concepts can play an important role in evaluating three key factors in EGS: conductivity, connectivity, and conformance.

5. CONCLUSION

In this study, we proposed a computationally efficient, streamline-based workflow for fracture property calibration in enhanced geothermal systems (EGS) and demonstrated the utility of streamlines for visualization and reservoir flow analysis in EGS. The key findings are summarized below.

- A novel streamline-based inversion framework is introduced for geothermal applications by tailoring a well-established oil and gas technology to EGS. The streamline formulation enables efficient computation of sensitivities of the observed responses (distributed temperature and distributed flow rate data along the horizontal well) with respect to fracture properties from a single forward simulation, thereby reducing the number of required forward simulations for model calibration and accelerating the inversion workflow.

- The proposed workflow was validated using a synthetic case and the Utah FORGE field case, demonstrating efficient calibration of fracture properties using available observed data. In the synthetic case, cell-level DTS and flow rate data were assimilated, whereas in the Utah FORGE application, cluster-level flow rate data were assimilated. The high computational efficiency of the framework enabled completion of the field-scale fracture calibration in approximately one day.

- Streamlines and thermal tracer travel time are shown to be effective visualization tools for evaluating three key factors in EGS: fracture conductivity, connectivity, and flow conformance. Permeability updates from the inversion process illustrate changes in conductivity; destination-colored streamline visualizations show how injector-producer connectivity and cluster-level flow allocation change during calibration; and thermal tracer travel time visualizations provide insight into reservoir conformance and thermal breakthrough time.

ACKOWLEDGEMENTS

This work is supported by the members of the Texas A&M Joint Industry Project, Model Calibration and Efficient Reservoir Imaging (MCERI).

REFERENCES

Aladwani, Heba, Hussain, Sadam, Fahes, Mashhad et al. 2025. Novel Reactive Tracer Injection for Tracking Thermal Front Propagation. *Industrial & Engineering Chemistry Research* **64** (19): 9656-9670. https://doi.org/10.1021/acs.iecr.5c01242.

Allis, R., Moore, J., Davatzes, N. et al. 2016. EGS Concept Testing and Development at the Milford, Utah FORGE Site. Paper presented at the Proceedings of the 41st Workshop on Geothermal Reservoir Engineering, Stanford University, Stanford, California.

Alvaro, Rey, Akhil, Datta-Gupta, and Ballin, Paulo. 2011. Assisted history matching in the presence of frequent well intervention using generalize travel time inversion. *Journal of Petroleum Science and Engineering* **78** (2): 415-430. https://www.sciencedirect.com/science/article/pii/S0920410511001288.

Bjarkason, Elvar K. 2023. How precise can thermal breakthrough predictions be that are derived from adsorptive tracer tests? *Proc.*, Proceedings, 48th Workshop on Geothermal Reservoir Engineering, Stanford University, Stanford, California, February 6-8, 2023, Stanford, California.

Cao, Meng and Sharma, Mukul. 2023a. An Efficient Model of Simulating Fracture Propagation and Energy Recovery from Naturally Fractured Reservoirs: Effect of Fracture Geometry, Topology and Connectivity. *Proc.*, SPE Hydraulic Fracturing Technology Conference and Exhibition. https://doi.org/10.2118/212315-MS.

Cao, Meng and Sharma, Mukul M. 2022. The impact of changes in natural fracture fluid pressure on the creation of fracture networks. *Journal of Petroleum Science and Engineering* **216**: 110783. https://www.sciencedirect.com/science/article/pii/S0920410522006453.

Cao, Meng and Sharma, Mukul M. 2023b. Creation of a Data-Calibrated Discrete Fracture Network of the Utah FORGE Site. *Proc.*, 57th U.S. Rock Mechanics/Geomechanics Symposium. https://doi.org/10.56952/ARMA-2023-0822.

Cao, Meng and Sharma, Mukul M. 2023c. Factors Controlling the Flow and Connectivity in Fracture Networks in Naturally Fractured Geothermal Formations. *SPE Drilling & Completion* **38** (01): 131-145. https://doi.org/10.2118/212292-PA.

Cao, Meng and Sharma, Mukul M. 2023d. Geomechanical Modeling of Fracture Growth in Naturally Fractured Rocks: A Case Study of the Utah FORGE Geothermal Site. *Proc.*, SPE/AAPG/SEG Unconventional Resources Technology Conference. https://doi.org/10.15530/urtec-2023-3864731.

Chan, Chin-Hsiang, Datta-Gupta, Akhil, and Shor, Roman J. 2025. Fast Marching Method: A New Paradigm for Rapid Simulation of Enhanced Geothermal Systems. Paper presented at the Proceedings of the 50th Workshop on Geothermal Reservoir Engineering, Stanford University, Stanford, California, February.

Chan, Chin-Hsiang, Kumawat, Piyush Kumar, Deo, Milind et al. 2025. Dynamic Reservoir Modeling of the Utah FORGE Enhanced Geothermal Project Using Fast Marching Method. *Proc.*, SPE Energy Transition Symposium. https://doi.org/10.2118/228338-MS.

Chen, Hongquan, Yang, Changdong, Datta-Gupta, Akhil et al. 2019. A Hierarchical Multiscale Framework for History Matching and Optimal Well Placement for a HPHT Fractured Gas Reservoir, Tarim Basin, China. *Proc.*, International Petroleum Technology Conference. https://doi.org/10.2523/IPTC-19314-MS.

Chen, Hongquan, Yang, Changdong, Datta-Gupta, Akhil et al. 2020. Fracture inference and optimal well placement using a multiscale history matching in a HPHT tight gas reservoir, Tarim Basin, China. *Upstream Oil and Gas Technology* **2**: 100002. https://www.sciencedirect.com/science/article/pii/S2666260420300025.

Chen, Hongquan, Yao, Changqing, Datta-Gupta, Akhil et al. 2020. Identification of Fractures and Preferential Flow Paths Using Streamlines and Dynamic Data in Dual Porosity Dual Permeability Reservoir Models. *Proc.*, SPE Annual Technical Conference and Exhibition. https://doi.org/10.2118/201277-MS.

Chen, Yuedu and Zhao, Zhihong. 2020. Heat transfer in a 3D rough rock fracture with heterogeneous apertures. *International Journal of Rock Mechanics and Mining Sciences* **134**: 104445. https://www.sciencedirect.com/science/article/pii/S1365160920308145.

Cheng, Hao, Datta-Gupta, Akhil, and He, Zhong. 2005. A Comparison of Travel-Time and Amplitude Matching for Field-Scale Production-Data Integration: Sensitivity, Nonlinearity, and Practical Implications. *SPE Journal* **10** (01): 75-90. https://doi.org/10.2118/84570-PA.

Cheng, Hao, Oyerinde, Dayo, Datta-Gupta, Akhil et al. 2007. Compressible Streamlines and Three-Phase History Matching. *SPE Journal* **12** (04): 475-485. https://doi.org/10.2118/99465-PA.

Dadi, Sireesh, Norbeck, Jack, Titov, Aleksei et al. 2024. Microseismic Monitoring of a Horizontal EGS System: Case Study and State of the Art. *Proc.*, Proceedings, 49th Workshop on Geothermal Reservoir Engineering, Stanford University, Stanford, California, February 12-14, 2024 (SGP-TR-227). https://pangea.stanford.edu/ERE/db/GeoConf/papers/SGW/2024/Dadi.pdf.

Datta-Gupta, Akhil and King, Michael J. 2007. *STREAMLINE SIMULATION: THEORY AND PRACTICE*: SPE TEXTBOOK SERIES VOL. 11.

England, Kevin, Swearingen, Leroy, and McLennan, John. 2024. Utah FORGE: Wells 16A(78)-32 and 16B(78)-32 Extended Circulation Test DAta - August and September 2024.

Finnila, Aleta and Jones, Clay. 2024. Utah FORGE: 2024 Discrete Fracture Network Model Data, Energy and Geoscience Institute at the University of Utah.

Fox, Don Bruce, Koch, Donald Lyle, and Tester, Jefferson William. 2015. The effect of spatial aperture variations on the thermal performance of discretely fractured geothermal reservoirs. *Geothermal Energy* **3** (1): 21. https://doi.org/10.1186/s40517-015-0039-z.

Fu, Pengcheng, Hao, Yue, Walsh, Stuart D. C. et al. 2016. Thermal Drawdown-Induced Flow Channeling in Fractured Geothermal Reservoirs. *Rock Mechanics and Rock Engineering* **49** (3): 1001-1024. https://doi.org/10.1007/s00603-015-0776-0.

Grant, Malcolm A. and Bixley, Paul F. 2011. *Geothermal Reservoir Engineering*: Elsevier.

Guo, Bin, Fu, Pengcheng, Hao, Yue et al. 2016. Thermal drawdown-induced flow channeling in a single fracture in EGS. *Geothermics* **61**: 46-62. https://www.sciencedirect.com/science/article/pii/S0375650516000067.

He, Zhong, Yoon, Seongsik, and Datta-Gupta, Akhil. 2002. Streamline-Based Production Data Integration With Gravity and Changing Field Conditions. *SPE Journal* **7** (04): 423-436. https://doi.org/10.2118/81208-PA.

Hetz, Gill, Kim, Hyunmin, Datta-Gupta, Akhil et al. 2017. History Matching of Frequent Seismic Surveys Using Seismic Onset Times at the Peace River Field, Canada. *Proc.*, SPE Annual Technical Conference and Exhibition. https://doi.org/10.2118/187310-MS.

Holt, Richard. 2025. EGS Well Test Analysis from the Perspective of Conventional Geothermal Reservoir Engineering. *Proc.*, Proceedings, 50th Workshop on Geothermal Reservoir Engineering, Stanford University, Stanford, California, February 10-12, 2025 (SGP-TR-229). https://pangea.stanford.edu/ERE/db/GeoConf/papers/SGW/2025/Holt.pdf.

Horne, Roland, Genter, Albert, McClure, Mark et al. 2025. Enhanced geothermal systems for clean firm energy generation. *Nature Reviews Clean Technology* **1** (2): 148-160. https://doi.org/10.1038/s44359-024-00019-9.

Ji, Kun, Li, Hong, and Liu, Sai. 2025. Mitigating thermal breakthrough in enhanced geothermal systems using nanofluids. *Proc.*, Proceedings, 50th Workshop on Geothermal Reservoir Engineering, Stanford University, Stanford, California, February 10-12, 2025 (SGP-TR-229), Stanford, California.

Jurick, Dana. 2024. Utah FORGE: Well 16B(78)-32 DTS, RFS DSS Strain, and Absolute Strain Circulation Test Fiber Optic Data - August 2024, Neubrex Energy Services (US), LLC (August 2024).

Jurick, Dana and Guzik, Artur. 2024. Utah FORGE: Well 16B(78)-32 DTS, RFS DSS Strain, and Absolute Strain Circulation Test Fiber Optic Data - August 2024.

Kumawat, Piyush Kumar, Panja, Palash, and Jin, Wencheng. 2025. Simplified Fracture Model for Numerical Simulation of EGS: A Utah FORGE Case Study. Paper presented at the Proceedings of the 50th Workshop on Geothermal Reservoir Engineering, Stanford University, Stanford, California, February.

Li, Ao, Chen, Hongquan, Jalali, Ridwan et al. 2024. From Streamline to Pathline: Visualizing Particle Trajectories Under Changing Velocity Fields. *SPE Journal* **29** (07): 3801-3812. https://doi.org/10.2118/215088-PA.

Liu, Qianjun, Cao, Meng, Ou, Yuhao et al. 2025. Hydraulic Fracturing Design in Geothermal Wells: A Utah FORGE Case Study. *Proc.*, SPE Hydraulic Fracturing Technology Conference and Exhibition. https://doi.org/10.2118/223548-MS.

Liu, Qianjun, Ou, Yuhao, and Sharma, Mukul. 2024. Factors Controlling the Properties of Hydraulic Fracture Networks in Naturally Fractured Formations. *Proc.*, SPE Annual Technical Conference and Exhibition. https://doi.org/10.2118/221065-MS.

Liu, Tian, Chen, Hongquan, Hetz, Gill et al. 2020. Integration of time-lapse seismic data using the onset time approach: The impact of seismic survey frequency. *Journal of Petroleum Science and Engineering* **189**: 106989. https://www.sciencedirect.com/science/article/pii/S0920410520300851.

McClure, Mark. 2023. Calibration Parameters Required to Match the Utah FORGE 16A(78)-32 Stage 3 Stimulation with a Planar Fracturing Model. Paper presented at the Proceedings of the 48th Workshop on Geothermal Reservoir Engineering, Stanford University, Stanford, California, February.

Paige, Christopher C. and Saunders, Michael A. 1982. LSQR: An Algorithm for Sparse Linear Equations and Sparse Least Squares. *ACM Trans Math Softw* **8** (1): 43–71. https://doi.org/10.1145/355984.355989.

Parker, Robert L. 1994. *Geophysical inverse theory*: Vol. 1: Princeton university press.

Podgorney, Robert. 2020. Utah FORGE: Data for 3-D Model Development - Lithology, Temperature, Pressure, and Stress, Idaho National Laboratory.

Podgorney, Robert, Munday, Lynn, and Finnila, Aleta. 2025. Thermo-Hydraulic Modeling of Long-Term Circulation Tests at the Utah FORGE Site. *Proc.*, Proceedings, 50th Workshop on Geothermal Reservoir Engineering, Stanford University, Stanford, California, February 10-12, 2025 (SGP-TR-229). https://pangea.stanford.edu/ERE/pdf/IGAstandard/SGW/2025/Podgorney.pdf.

Pollock, David W. 1988. Semianalytical Computation of Path Lines for Finite-Difference Models. *Groundwater* **26** (6): 743-750. https://ngwa.onlinelibrary.wiley.com/doi/abs/10.1111/j.1745-6584.1988.tb00425.x.

Potter, Robert M., Smith, Morton C., and Robinson, Eugene S. 1974. Method of extracting heat from dry geothermal reservoirs. United States Patent Application No. US 3,786,858.

Sagbana, Perekaboere Ivy and Abushaikha, Ahmad Sami. 2021. A comprehensive review of the chemical-based conformance control methods in oil reservoirs. *Journal of Petroleum Exploration and Production Technology* **11** (5): 2233-2257. https://doi.org/10.1007/s13202-021-01158-6.

Schölderle, Felix, Lipus, Martin, Pfrang, Daniela et al. 2021. Monitoring cold water injections for reservoir characterization using a permanent fiber optic installation in a geothermal production well in the Southern German Molasse Basin. *Geothermal Energy* **9** (1): 21. https://doi.org/10.1186/s40517-021-00204-0.

SLB. 2023. *ECLIPSE Technical description Version 2023.2*. Houston, Texas, USA: SLB.

Smith, Morton C., Potter, Robert M., Brown, Donald W. et al. 1973. Induction and growth of fractures in hot rock. In *Geothermal Energy: Resources, Production, Stimulation*, ed. Paul Kruger and Carel Otte, 251-265. Stanford, California: Stanford University Press.

Somogyvári, M., Bayer, P., and Brauchler, R. 2016. Travel-time-based thermal tracer tomography. *Hydrol Earth Syst Sci* **20** (5): 1885-1901. https://hess.copernicus.org/articles/20/1885/2016/.

Srinivasan, Aishwarya, Wu, Kan, Jin, Ge et al. 2025. Characterizing Fracture Geometry Using Integrated Fiber-Optic Strain Data from Horizontal and Vertical Monitoring Wells: A Case Study in Enhanced Geothermal Systems. *Proc.*, SPE/AAPG/SEG Unconventional Resources Technology Conference. https://doi.org/10.15530/urtec-2025-4258573.

Tanaka, Shusei, Kam, Dongjae, Datta-Gupta, Akhil et al. 2015. Streamline-Based History Matching of Arrival Times and Bottomhole Pressure Data for Multicomponent Compositional Systems. *Proc.*, SPE Annual Technical Conference and Exhibition. https://doi.org/10.2118/174750-MS.

Titov, Aleksei, Shako, Valery, Kortukov, Dmitrii et al. 2025. Fiber Optic Model Based Flow Quantification Enhancing Geothermal Systems. *Proc.*, Proceedings, 50th Workshop on Geothermal Reservoir Engineering, Stanford University, Stanford, California, February 10-12, 2025 (SGP-TR-229). https://pangea.stanford.edu/ERE/pdf/IGAstandard/SGW/2025/Titov.pdf.

Wagner, W., Cooper, J. R., Dittmann, A. et al. 2000. The IAPWS Industrial Formulation 1997 for the Thermodynamic Properties of Water and Steam. *Journal of Engineering for Gas Turbines and Power* **122** (1): 150-184. https://doi.org/10.1115/1.483186.

Watanabe, Shingo, Han, Jichao, Hetz, Gill et al. 2017. Streamline-Based Time-Lapse-Seismic-Data Integration Incorporating Pressure and Saturation Effects. *SPE Journal* **22** (04): 1261-1279. https://doi.org/10.2118/166395-PA.

Wu, Hui, Fu, Pengcheng, Hawkins, Adam J. et al. 2021. Predicting Thermal Performance of an Enhanced Geothermal System From Tracer Tests in a Data Assimilation Framework. *Water Resources Research* **57** (12): e2021WR030987. https://agupubs.onlinelibrary.wiley.com/doi/abs/10.1029/2021WR030987.

Xing, Pengju, England, Kevin, Moore, Joseph et al. 2025. Analysis of the 2024 Circulation Tests at Utah FORGE and the Response of Fiber Optic Sensing Data. *Proc.*, Proceedings, 50th Workshop on Geothermal Reservoir Engineering, Stanford University, Stanford, California, February 10-12, 2025 (SGP-TR-229). https://pangea.stanford.edu/ERE/pdf/IGAstandard/SGW/2025/Xing2.pdf.

Yang, Changdong, Xue, Xu, King, Michael J. et al. 2017. Flow Simulation of Complex Fracture Systems With Unstructured Grids Using the Fast Marching Method. *Proc.*, Unconventional Resources Technology Conference, Austin, Texas, 24-26 July 20172683-2700. https://doi.org/10.15530/urtec-2017-2691393.

Yao, Changqing, Chen, Hongquan, Onishi, Tsubasa et al. 2024. Robust CO2 plume imaging by joint tomographic inversion using distributed pressure and temperature measurements. *International Journal of Greenhouse Gas Control* **135**: 104166. https://www.sciencedirect.com/science/article/pii/S1750583624001099.

Yin, Jichao, Park, Han-Young, Datta-Gupta, Akhil et al. 2011. A hierarchical streamline-assisted history matching approach with global and local parameter updates. *Journal of Petroleum Science and Engineering* **80** (1): 116-130. https://www.sciencedirect.com/science/article/pii/S0920410511002701.

Zhang, Ruxin, Park, Jaeyoung, Nunna, Krishna et al. 2025. Streamline-Based Three-Phase History Matching for Field-Scale Compositional Modeling Under CO2 Enhanced-Oil-Recovery in the Permian Basin, Texas. *Proc.*, SPE Reservoir Simulation Conference. https://doi.org/10.2118/223883-MS.